Experimental investigation on the performance analysis and internal flow characteristics inside the vane-island diffuser of centrifugal pumps at several flow rates

Qiaorui Si[1], Shouqi Yuan
siqiaorui@gmail.com, shouqiy@ujs.edu.cn
National Research Center of Pumps, Jiangsu University

Patrick Dupont
Patrick.Dupont@ec-lille.fr
LML, UMR CNRS 8107, Ecole Centrale de Lille

Annie-Claude Bayeul-Lainé, Antoine Dazin, Olivier Roussette
annie-claude.bayeul@lille.ensam.fr, antoine.dazin@lille.ensam.fr, Olivier.ROUSSETTE@ensam.EU
LML, UMR CNRS 8107, Arts et Métiers Paristech

ABSTRACT

Measurements are processed on a centrifugal pump model, which works with air and performs with the vane-island type diffuser of a real hydraulic pump, under five flow rates to investigate the internal flow characteristics and their influence on overall pump performance. The mean flow characteristics inside the diffuser are determined by using of a miniature three-hole probe connected to an online data acquisition system. The flow structure at the inlet section of the diffuser is analyzed in detail, with a focus on the local pressure loss inside the vane less gap and incidence angle distributions along the hub-to-shroud direction of the diffuser. Some existing URANS calculations, including leakage effects, are used to evaluate the pressure recovery downstream of the impeller. Furthermore, 2D/2C high-speed stereoscopic PIV measurement results are obtained to help analyze the flow characteristics inside the vane-island diffuser. Each PIV measuring plane is related to one particular diffuser blade-to-blade channel and is analyzed by using the time-averaged method according to seven different relative positions of the impeller. Measurement results show that main loss is produced inside the vane less part of the diffuser at low flow rates, which might have been caused by the strong rotor–stator interaction. When the impeller flow rate is greater than the diffuser design flow rate, a large fluctuating separated region occurs after the throat of the diffuser on the pressure side. Mean loss originates from the unsteady pressure downstream of the diffuser throat. For better characterization of the separations observed in previous experimental studies, complementary unsteady static pressure measurement campaigns have been conducted on the diffuser blade wall. The unsteadiness revealed by these measurements, as well as theirs effects on the diffuser performance, was then studied.

Keywords: vane-island diffuser; mean flow characteristics; three-hole probe; PIV; flow separation

---

[1] National Research Center of Pumps, Jiangsu University, Zhenjiang city, China, 212013

1. Introduction

Centrifugal pumps are essential energy conversion devices and fluid-transporting equipment. One of the great astronomical projects of centrifugal pumps is to increase the machine performance in this competitive and energy conscious world. However, flow inside a centrifugal vane pump is three-dimensional, turbulent, and always associated with strong rotor–stator interaction, as highlighted in previous works [1–3]. Thus, solid knowledge of the flow characteristics within the impeller and diffuser is indispensable to improve the hydraulic performance of centrifugal pumps.

Flow in the vaned diffuser radial pump is characterized by a strong jet–wake flow structure from the impeller and unsteady interactions between the rotating impeller and the stationary diffuser. Such interactions result in large pressure fluctuations both downstream and upstream. These fluctuations not only generate noise and vibration but also bring unfavorable pump performance even at the design point [4–7]. Diffuser pump performance improves with the reduction of flow losses in the diffuser, which yields high pressure recovery, and in the impeller [8]. Despite considerable experimental and numerical studies conducted on the flow downstream of the impeller [9–14], findings remain insufficient to facilitate understanding of the flow mechanism inside the diffuser and the interaction effect from the impeller and diffuser blades. In our previous works on the same model, complementary PIV measurements and numerical simulation had been used in a special pump working with air. These published works include those by Wuibaut et al. [15], Atif et al. [16], Dazin et al. [17], and Cavazzini et al. [18, 19]. Comparisons between PIV and full URANS calculation results in the present pump model have been discussed, with consideration of the impeller blade location relative to the vane diffuser channel. However, previous studies only focused on the unsteady velocity fields inside the impeller channel. Further studies that consider the pressure recovery downstream of the impeller and the development gradients of vortex flow are required to analyze the effect of internal flow characteristics on overall pump performance. In a research loop model, only an

intrusive directional pressure probe traverse enables total pressure evaluation and consequently corrects impeller and pump loss evaluations.

In this study, a classical three-hole probe was used to cover most of the complete flow passage of the diffuser. The overall performance of the pump model was presented. The pressure recovery downstream of the impeller was analyzed by using the mean values at the impeller outlet derived from pre-existing torque measurements and unsteady calculation results as the inlet flow conditions. Complementary PIV measurement associated with the unsteady blade wall static pressure test in one diffuser blade-to-blade passage was used to describe the fundamental flow characteristics of vane-island radial pumps. The effects of flow separation on overall pump performance were also discussed.

2. Experimental apparatus and overall pump performance measurement

2.1 Pump dimensions

The experiments were conducted on a pump working with air and under conditions similar to those in water. The pump is composed of an SHF impeller matched with a vaned diffuser, the characteristics of which are listed in Table 1. No volute was used downstream of the diffuser to focus the analysis on the rotor–stator interaction. The diffuser design flow rate corresponds to 80% of the impeller design flow rate ($Q_n = 0.3365$ m^3/s). This configuration has been chosen to enhance performance when the pump operates at partial working condition. The outlet parts of the impeller and of the entire diffuser are characterized by a two-dimensional design.

2.2 Process of global measurement

The system diagram and the main specifications of the test apparatus are shown in Fig. 1. An aspiration circuit consists of a pipe and an aspiration caisson. The operating conditions were regulated with normalized diaphragms positioned on a wall of the caisson. Calculating the flow rate in the pipe was made possible by

measuring the pressure difference between upstream and downstream of the diaphragm. The mass flow in the caisson moved through a honeycomb filter and finally entered the aspiration pipe. An asynchronous motor of 5.5 kW coupled with a speed variator was used to drive the pump. The exact impeller rotation velocity was measured by using a numeric stroboscope BRUEL ET KJAER Type 4913 coupled with a photoelectric cell. The pressure measurements (at the impeller inlet and in the aspiration caisson) were conducted with the use of a Selector BEXHILI 20 pneumatic channel and a digital manometer YEW type 2654. The temperature and relative humidity were determined at the machine exit by using a digital thermohygrometer DOSTMANN T870 to calculate air density.

A miniature three-hole probe was used to measure the mean flow characteristics downstream of the impeller. Measurements were conducted at 23 positions, as shown in Fig. 1(c), at five mass flow rates. For each blade-to-blade position, axial traverse was performed from hub to shroud to cover a complete flow distribution section inside the diffuser plane. The three-hole probe is connected to the honeywell type pressure sensor, which transforms pressure tension information in a real-time online data acquisition system controlled by LabVIEW. Every pressure transducer is calibrated to obtain a calibration certificate before measurement.

2.3 Three-hole probe measurement method

Flow direction can generally be precisely determined by using the null method for probe measurement. This method equalizes the pressure on two opposite static tappings. However, it has low efficiency in obtaining an improved value in the test diffuser because the approach requires several attempts to rotate the setting angle owing to the low reference pressure. In the non-nulling method, the probe is mounted at a fixed position, and the flow characteristic values are calculated through prior calibration. However, this method is sensitive to the probe characteristics. Calibration and data processing were carefully conducted to ensure the validity of the measured angles within the Reynolds number range [20]. Moreover, calibration measurement

should be conducted to ensure a useful range of the pitch and yaw angles and to establish the zero point. During our calibration, three coefficients were defined to represent the probe characteristics. The pitch and yaw angles were changed from -33° to 33°, with an interval of 3° at four Reynolds numbers (using probe diameter as the reference length). The results shown in Fig. 2 indicate that the angle calibration coefficient C_α of Reynolds number dependency is significant, whereas the pressure coefficient C_{po} and velocity coefficient C_{ps} are insignificant. The Reynolds number effects on the pitch and yaw angle coefficient C_α are negligible when the absolute values of the pitch and yaw angles are less than 13°, such that a linear variation is observed. Therefore, an economical method combining the semi-null method with the calibration curve was adopted in our measurement with a focus on setting C_a to be less than 1.

$$C_\alpha = \frac{P_l - P_r}{P_c - 0.5 \times (P_l + P_r)} \tag{1}$$

$$C_{p0} = \frac{P_{tot} - P_c}{P_c - 0.5 \times (P_l + P_r)} \tag{2}$$

$$C_{ps} = \frac{P_{tot} - P_{sta}}{P_c - 0.5 \times (P_l + P_r)} \tag{3}$$

3. Mean flow characteristic results

3.1 Pump component performance curves and leakage calculation

To analyze the diffuser performance, the impeller outlet conditions have to be determined. The overall performance curve of the impeller is deduced from the experimental results obtained by Barrand et al. [21], as shown in Fig. 3. These results have been validated in two different water test stands, namely INSA de Lyon (Villeurbanne, France) and EPFL Lausanne (Lausanne, Switzerland). The straight line corresponding to the theoretical curve correctly fits the first curve with an extensive flow rate range. This straight line was obtained by applying the Euler equation, with the assumption that no swirl velocity exists at the impeller inlet and that a constant outlet relative angle β_2 is equal to 14° with the tangential direction. The existing experimental impeller head curve enabled the calculation of the mean absolute tangential velocity outside

the impeller. The mean radial velocity was from the division of the flow rate and the section area of the impeller exit. Impeller efficiencies were determined from existing 1D loss models, the results of which were similar to those obtained by using unsteady loss calculations from several CFD methods. The calculated real fluid total and static pressure coefficient at the impeller outlet for five chosen flow rates are also shown in Fig. 3. These values were taken as the initial conditions for all further performance evaluations downstream of the impeller.

The non-dimensional pump head curves shown in Fig. 3 correspond to global performance in terms of total pressure coefficient. The total pressure coefficient was calculated after obtaining the static pressure in the tank and at the inlet of the impeller. Moreover, the test process was conducted under four operating rotational speeds. The results are also shown in Fig. 3. On the basis of the results, we can conclude that the Reynolds number insignificantly affects the flow structure inside the pump under the four rotating speeds. This result would help us use the similarity law in turbomachinery and avoid the limit of the pressure sensor.

Given that temperature is of significant importance relative to air density, considerable attention was focused on the measurement to ensure that all test results were collected within a 2 C temperature variation. After probe measurement and weight average solution calculation, the mean values of total pressure at the inlet and outlet of the diffuser can be obtained. Diffuser performance is shown in Fig. 3, where non-dimensional total pressure change linearly decreases as flow increases.

During measurement, the global flow rate must be considered when determining the pump operating conditions. For the present experimental setup, two main types of leakage exist in the operating pump model, as shown in Fig. 4. The global flow rate of the impeller is the sum of the flow rate in the caisson Q_{vc} and the leakage flow rate Q_{vl}, which can be calculated by using Formulas 4 and 5:

$$Q_{vc} = \delta S \sqrt{\frac{2\Delta P_c}{\rho}} \qquad (4)$$

$$Q_{vl} = 5.4494 \times 10^{-3} \sqrt{\frac{2\Delta P_i}{404\rho}} \qquad (5)$$

where δ is the flow rate coefficient of the diaphragm, S is the area of the diaphragm section, ΔP_c is the pressure difference between upstream and downstream of the diaphragm, ρ is the air volumetric density, and ΔP_i is the difference between the atmospheric and wall pressures at the impeller inlet.

The flow rate in the diffuser is the sum of three parts, namely, the flow from the impeller Q_{imp}, the leakage flow from the shroud Q_{shroud}, and the leakage flow from the hub Q_{hub}. A specific arrangement enables flow leakage just after the impeller outlet section. The low pressure may cause this leakage to enter into the vane diffuser. Based on the Bernoulli equation, the following recursion formulas can be used to calculate the leakage flow:

$$\Delta P_{shr} = \frac{\lambda \cdot l}{D_h} \cdot 0.5\rho V_{z,shr}^2 + \left(K_{ret} + K_{el}\right) \cdot 0.5\rho V_{z,shr}^2 \qquad (6)$$

$$\Delta P_{hub} = \left(2K_{count90} + K_{ret} + K_{el}\right) \cdot 0.5\rho V_{z,hub}^2 \qquad (7)$$

$$Q_{diff} = Q_{imp} + S \cdot V_{z,shr} + S \cdot V_{z,hub} \qquad (8)$$

Based on the impeller total head coefficient curve shown in Fig. 3, the mean total pressure outside the impeller can be obtained. After integrating the relevant geometric parameter of the leakage channel and pressure difference into Formulas 6, 7, and 8, the leakage flow rate can be calculated. The values of the coefficients in these formulas can be derived from [22]. The non-dimensional flow rate of pump components is shown in Fig. 5. The leakage at the impeller inlet is always positive and maintains a constant percentage with increasing flow rate. Inward impeller tip leakage flow always occurs when the non-dimensional mass flow rate of the impeller is less than 0.8, whereas outward leakage flow occurs at $0.956Q_n$ and $1.12Q_n$. The impeller tip leakage flow reaches its maximum of approximately 28% at $0.386Q_n$, which will significantly affect the flow field. The conclusions are in accordance with the existing numerical simulation results, including leakage effects [23]. In detail, as shown in Fig. 3, the non-dimensional head curve of the impeller separates the theoretical line that is approximately 0.7 times the impeller design flow rate. This result indicates that revolution flow at the impeller import will occur and increase with decreasing flow rate. Given

that no pre-rotate assumption was used in calculating the value of leakage, the obtained result was relatively large.

3.2 Probe measurement results at the diffuser inlet

Flow inside the diffuser can be divided into two parts, namely, the vane less and vaned blade parts. Nine probe measurement points for five different flow rates are placed at the inlet of the diffuser to evaluate the flow characteristic at the vane less part. The probe dimensions make it difficult to perform accurate measurements at points 1 and 9, which respectively correspond to the pressure and suction sides. The flow information calculated from points 2 to 8 is accurate, as shown from Figs. 6 to 10. The nondimensional pressure coefficient calculated from ambient flow conditions (P_{atm}, ρ), the static pressure at the inlet pipe (P_{aspA}), and the rotor tip velocity (u_2) can be expressed as:

$$v^* = v/u_2 \qquad (9)$$

$$\mathrm{d}P_{tot}^* = \frac{P_{tot} - P_{aspA\text{-}tot}}{0.5\rho u_2^2} \qquad (10)$$

$$\mathrm{d}P_{sta}^* = \frac{P_{sta} - P_{aspA}}{0.5\rho u_2^2} \qquad (11)$$

As shown in Fig. 6, the mean value of the flow angle decreases with increasing flow rates. Angles greater than 90° indicate backflow from the vane diffuser part. These places locate near the shroud and hub side and disappear as flow rate increases. This reverse flow region even corresponds to 20% of the diffuser width at a close diffuser design flow rate $Q/Q_n = 0.762$ and is associated with low absolute mean velocities, as shown in Fig. 8. Fig. 7a shows the average incidence flow angle distribution from the hub-to-shroud section for five mass flow rates, which were obtained from the difference between the absolute flow angle α and the diffuser blade angle (79.8°). Negative incidence was observed in the middle of the height section. For low flow rates, negative incidence values were evident because of strong blockage effects near the shroud with high positive incidence values. Low incidence values were observed for the two highest flow rates because radial velocity distribution was almost constant over the hub-to-shroud section, as shown in

Fig. 7b.

As shown in Fig. 8, cores with high kinetic energy move from the suction side to the pressure side and then remain near the mid-span as flow rate increases. Similarly, the non-dimensional static pressure distribution maps shown in Fig. 9 indicate that places with low static pressure move from the suction side to the pressure side. Low values are concentrated in the middle of the passage with an almost equivalent pressure level close to the pressure and suction sides when flow conditions are close to the design point of the vane diffuser. The maximum non-dimensional absolute velocities decrease with increasing flow rate, which is in accordance with the non-dimensional static pressure distribution. As shown in Fig. 10, maximum total pressure levels are located at the mid-span diffuser width and in the middle part of the blade-to-blade section toward the pressure side. For $Q/Q_n = 0.762$, the maximum total pressure coefficient value obtained by the probe measurements exactly corresponds to the mean total pressure value calculated at the impeller outlet section, as shown in Fig. 3. This finding indicates that after mixing, a blade-to-blade loss distribution is obtained in the vane less diffuser part with consideration of the downstream vane diffuser interactions. The corresponding maximum total pressure zone is then equivalent to the isentropic flow conditions inside the vane less diffuser part originating from the impeller outlet condition. This result also corresponds to a time-averaged total pressure distribution because the combination of rotor–stator interactions and jet–wake structure that originates from the impeller itself causes unsteady flow in this region.

3.3 Probe measurement results along the diffuser mean line

To investigate the behavior of the vaned diffuser and the evolution of the phenomena in the analyzed diffuser passage, we must determine the mean line and analyze its flow characteristics. In this investigation, the perpendiculars to the blade surfaces were constructed. The intersection point between the two perpendiculars, at equal distance from the blade surfaces, is then identified. These points, including points 19 to 23, are used to construct the mean line. Contours of static pressure distribution located at the mean line

from the inlet to the outlet in the diffuser are determined for five flow rates, as shown in Fig. 11. The static pressure is always higher near the shroud than the hub. Low pressure area cores move downstream with increasing flow rate and park in the throat of the diffuser.

During testing, points from 10 to 15 and point 18 are unpredictable. For points 10, 11, 12, 13, and 18, this unpredictability may be attributed to the wall effects when the probe is located extremely close to the wall. For points 14 and 15, the unpredictable flow might be caused by the strong flow separation around the pressure side of diffuser trailing edge. The sectional area of the diffuser channel increases, which results in an adverse pressure gradient and a sudden separation of the boundary layer.

A more detailed analysis of diffuser performance is proposed in Fig. 12, which shows the mean static pressure evolution with radius downstream of the impeller. Initial pressure and velocity values are derived from the impeller outlet conditions, as stated in Section 3.1. This figure clearly shows that the diffuser can be divided into two regions. In the vane less part, static pressure slightly increases for low flow rates $Q/Q_n =$ 0.386 and 0.583. This result is linked to the sudden deceleration of the diffuser inlet flow conditions, as shown in Fig. 9. For all other flow rate values, static pressure remains constant in the diffuser part. For Q/Q_n = 0.762, the static pressure value remains constant up to the diffuser throat that corresponds to positions 19 and 20. For Q/Q_n = 0.386 and 0.581, the static pressure increases rapidly before position 20 and then increases gradually. For the maximum flow rate value Q/Q_n = 1.12, no pressure recovery occurs mainly because of the negative incidence at the leading edge. This negative incidence is associated with strong local flow blockage, which results in strong acceleration in the vane diffuser channel associated with pressure losses. Moreover, as shown in Fig. 12, the theoretical pressure recovery factor determined by Formula 12 was plotted on the basis of the vane diffuser geometrical section evolution along the radius. In the following equation, v_R denotes the absolute velocity at radius R, and S is the area of the section at radius R:

$$\frac{\Delta P_s'}{0.5\rho v_2^2} = 1 - \frac{v_R^2}{v_2^2} = 1 - \left(\frac{S}{S_2}\right)^2 \cdot \frac{1+\tan^2\alpha(R)}{1+\tan^2\alpha(R_2)} \qquad (12)$$

By calculating the difference between the ideal and real measured final values, we conjecture that the negative values at flow rates of 0.968 and 1.12 before the diffuser throat may be caused by the leakage flow, which adds energy to the diffuser part. These differences also correspond to the total loss coefficient. The minimum loss condition locates between the diffuser design point and impeller design flow rate.

4 PIV measuring verification

The flow field inside the diffuser was also studied by using a 2D/2C high-speed PIV. These results were not only used to verify the probe experiment results but also to analyze the unsteadiness of the flow field.

4.1 PIV experimental setup

Some information on the PIV measuring system is shown in Fig. 13. Two complementary metal–oxide–semiconductor cameras (1,680 $\times$ 930 pixel^2), equipped with 50 mm lenses, were properly synchronized with the laser pulses. The angle between the object and image planes was approximately 45°. The laser illumination system consists of two independent Nd:YAG laser cavities, each producing an approximately 200 mJ/pulse at a frequency of 14.25 Hz. A light sheet approximately 90 mm wide with a thickness of 1.5 mm was obtained at five heights, including the mid-span. The experimental procedure enabled the determination of the mean absolute velocities in two exposure frames for up to seven different impeller angular positions relative to the diffuser vanes. More details on the PIV techniques used, experimental setup, and result interpretations can be found in [17].

4.2 Velocity results from PIV measuring

Image treatment was performed by using the software developed by the Laboratoire de Mecanique de Lille. For a given flow rate, this procedure enables us to obtain an overview of the phase-averaged absolute velocities inside the flow fields at each impeller angular position by means of contours. To obtain a better interpretation of the results, the radial and tangential components of the flow velocities in turbomachinery

must be determined. A procedure allowing for the determination of the impeller axis of rotation in the measuring plane has been developed. This procedure enabled the presentation of a highly precise analysis of the flow within the diffuser with velocity components for each impeller relative position at several spans. Examples at the mid-span that correspond to several blade-to-blade positions are shown in Table 2.

As shown in the table, the radial and tangential component evolution for every angular position resembles a cycle of one blade passage. Discrepancies can be observed during boundary layer development in the sections of two blade sides. Moreover, vortexes are identified at the diffuser entrance. The radial component always has three cores. When the impeller blade approaches the diffuser leading edge, the coherent vortices arrive from the impeller near the diffuser passage. The incoming fluctuations mix with the coherent large-scale structure created on the blade suction side. These fluctuations occur at half of the diffuser passage length when another core enters the diffuser inlet. All these fluctuations can be explained by the physical flow phenomenon called jet–wake and its interaction with the downstream diffuser. The waves emitted near the impeller trailing edge travel downstream and generate disturbances in the region of the diffuser leading edge.

To capture and visualize the unsteady flow field associated with the experimental comparison of mean flow characteristics, the appropriate method to measure velocity fields was developed according to equations 13 and 14. Finally, contours referring to the blade-to-blade evolutions of non-dimensional mean velocities and mean radial and tangential velocity components are shown in Table 3.

$$v_r = \frac{\int_{\theta_1}^{\theta_7} v_r(\theta)\,\mathrm{d}\theta}{\int_{\theta_1}^{\theta_7} \theta\,\mathrm{d}\theta} \qquad (13)$$

$$v_u = \frac{\int_{\theta_1}^{\theta_7} v_u(\theta)\cdot v_r(\theta)\,\mathrm{d}\theta}{\int_{\theta_1}^{\theta_7} v_r(\theta)\,\mathrm{d}\theta} \qquad (14)$$

As shown in Table 3, negative radial velocity components can be observed under diffuser design flow

rates. Interaction effects are apparently more important at smaller flow rates. After the throat section, strong mean velocity decelerations occur on the vaned pressure side because of the important negative incidence related to the increase in flow rate. The existing wake flow structure downstream of the impeller trailing edge is cut off by the leading edge of the diffuser, which causes strong flow fluctuations. Noticeable fluctuations in one impeller blade passage can be associated with the radial component distributions, which imply that a monopole acoustic source will partly contribute to the interactions. Fluctuations of the tangential velocity components are also observed. These fluctuations suggest that torque and/or pressure fluctuations on the blades will occur and result in dipole acoustic noise. Furthermore, the PIV results of the turbulence rate charts obtained from [24] at position 6 for several flow rates are shown in Fig. 14. In these charts, we consider only red zones of high turbulence (>10%) in the diffuser channel. In the impeller region, these areas should be neglected because they are representative of inconsistent values. At a low flow rate, the turbulence rate is moderate (<5%) in the entire domain, whereas a region of high turbulence appears at the pressure side with the flow rate increasing. This region also provides evidence of the separation of the boundary layer when flow rate is greater than the diffuser design flow rate according to [25]. We also note that the size of this zone fluctuates with the transpositional impeller position.

4.3 Comparison between two measuring results

A comparison of the experimental results between the three-hole probe and the PIV measurement are shown in Fig. 13. The results illustrate that velocity profiles and flow angles from probe measurement are in good agreement with the PIV experiment data. A slight difference between the seven positions of PIV measurement is observed when R/R_2 is greater than 1.25. Conversely, when R/R_2 is less than 1.25, relatively significant differences exist probably because of the strong flow disturbances caused by the rotor–stator interaction effect. The area of the flow passage becomes narrowest at this point, which may create high velocity gradients between the pressure and the suction sides of the diffuser channel. These gradients cannot

be measured by the probe itself. Furthermore, flow unsteadiness also causes angle error for probe measurement if established through probe calibration under stationary flow conditions. The method of probe measurement used in this study can help determine the mean real flow angle. Time-averaged values of velocity components from the PIV experiment verify the correctness of probe measurements although the unsteadiness yields higher velocity results for probe measurement.

5 Analysis of unsteadiness in the diffuser

To analyze the effect of flow separation-induced pressure fluctuations inside the vane diffuser, unsteady pressure measurements were conducted by using 8510B-1 Endevco pressure transducers. The transducers are located at five positions on the pressure face and four positions on the suction face of the diffuser in a blade-to-blade channel at mid-span, as shown in Fig. 16. The unsteady pressure measurements were performed with an acquisition time of 300 s and a sampling frequency of 6000 Hz. By using the Helmholtz resonance calculation, we determined that the natural frequency for the installed cavity of the sensor is 3070 Hz. Therefore, a low-pass filter was used with a 3000 Hz cut off frequency to avoid aliasing.

The statistical results of unsteady wall static pressure are shown in Fig. 17. From the root mean square (RMS) results, the levels of fluctuation decrease with increasing radius at the pressure side for all flow rates. The slope increases with increasing flow rate. Corresponding to the suction side, a steep increase is followed by a gradual decrease with increasing radius, which indicates that an area with significant unsteadiness exists. The RMS values at 0.968 Q_n and 1.12 Q_n are always larger both at the pressure and suction sides, which is associated with the separation area of the boundary layer. The averaged non-dimensional static pressure results at the pressure side almost present the same law as the probe measurement results at the mean line. The values increase with the radius and decrease with the flow rate. At the suction side, the values are constant at the diffuser design flow rate, which indicates less loss at this condition. Moreover, the values reveal the contrast variation between flow rates is greater than the diffuser design and smaller than

the diffuser design.

The auto power spectrum density (PSD) solution for pressure signals was achieved with the use of a 2048-point Hanning window with 50% overlap. The pressure pulsation in the frequency spectrum shown in Fig. 18 under five operating conditions indicate discrete spectral characteristics and blade passing frequency (199.5 Hz), with the multiples representing the main frequency. Peaks also appear at the impeller passing frequency (28.5) and its multiples. Peak values at the suction side are always greater than those at the pressure side, which can be attributed to the incidence angles. For point 9, the global increase in amplitude on a large-frequency band could be associated with increasing turbulence rate, especially at high flow rate. This global increase can be linked to the pulsations of the separated regions. By contrast, the spectrogram at point 6 did not present this characteristic. Moreover, peaks that are thrice the blade passing frequency (598.5) sometimes exhibit high values. This phenomenon is more evident at points located at the flow separation regions. A comprehensive effect was observed between the flow dynamic and the mechanical effect, which motivated us to conduct further studies.

6. Conclusions

Some experiments, including three-hole probe, PIV, and unsteady pressure measurements processed in the vane-island type diffuser of a centrifugal pump, are conducted in this study. The following conclusions are drawn from the experimental investigation:

1. Flow can be considered steady regardless of the relative position of the impeller, as long as overall diffuser performance is considered. Moreover, probe measurements enable the probe to rotate in such a way that pressure equilibrium is achieved between the two holes that are used to obtain the flow angle, which will partly avoid the error attributed to unsteadiness. The best pressure recovery factor is obtained near the design point of the diffuser that corresponds to the reduced flow rate value $Q/Q_n = 0.8$.

2. A large fluctuating separated region exists at the leading edge of the diffuser on the suction side at

low flow rates and at the trailing edge on the pressure side at high flow rates. This region induces an increase in the peak associated with the BPF and its harmonics, as well as a global increase in the pressure amplitude on a large-frequency band.

3. Noticeable fluctuations were observed in the radial component distributions and the impeller mean with a monopole hydroacoustic source to the spread of such a pump system. Fluctuations of the tangential velocity components indicate that pressure fluctuations on the blades will result in dipole sources of hydroacoustic noise, which would be the main type of noise in this pump system.

4. At low flow rates, turbulence cores, probably because of the rotor–stator interaction, originate from the impeller outlet, proceed into the diffuser passage, and decrease the probability density at the center of the diffuser passage and on the blade suction side. These conditions are the main reasons for performance loss. Moreover, the leakage flow enters the gaps and interacts with the impeller blade, which increases complexity. At high flow rates, loss always originates from the flow separation at the pressure side, and the areas of these regions become larger with increasing flow rates.

Acknowledgments

Nomenclature

θ: phase angle of the impeller blade

Tu: turbulence rate

α: flow angle

v_r: radial velocity

v_u: tangential velocity

v_R: absolute velocity at radius R

P_{aspA}: static pressure at the inlet pipe

D_h: equivalent diameter

l: length of leakage channel

λ, K_{ret}, K_{el}, $K_{coude90}$: discharge flow coefficient

References

[1] Sinha, M., Katz, J., 1999, "Quantitative visualization of the flow in a centrifugal pump with diffuser vanes Part I: on flow structures and turbulence," ASME J. Fluid Eng., **122**(1), pp. 97-107.

[2] Sinha, M., Katz, J., Meneveau, C., 1999, "Quantitative visualization of the flow in a centrifugal pump with diffuser vanes Part II: addressing passage-averaged and large-eddy simulation modeling issues in turbomachinery flows," ASME J. Fluid Eng., **122**(1), pp. 108-116.

[3] Majidi, K., 2005, "Numerical study of unsteady flow in a centrifugal pump," ASME J. Turbomach., **127**(2), pp. 363-371.

[4] Feng, J., Benra, F. K., Dohmen, H. J., 2010, "Unsteady flow investigation in rotor-stator interface of a radial diffuser pump," Forschung in Ingenieurwesen, **74**(4), pp. 233-242.

[5] Akin, O., Rockwell, D., 1994, "Actively controlled radial flow pumping system: manipulation of spectral content of wakes and wake-blade interactions," ASME J. Fluid Eng., **116**, pp. 528-536.

[6] Guleren, K. M., Pinarbasi, A., 2004, "Numerical simulation of the stalled flow within a vaned centrifugal pump," Proceedings of the Institution of Mechanical Engineers, Part C: Journal of Mechanical Engineering Science, **218**, pp. 425-435.

[7] Guo, S., Maruta, Y., 2005, "Experimental investigations on pressure fluctuations and vibration of the impeller in a centrifugal pump with vaned diffusers," JSME International Journal, Series B, **48**(1), pp. 136-143.

[8] Pavesi, G., Cavazzini, G., Ardizzon, G., 2008, "Time-frequency characterization of the unsteady phenomena in a centrifugal pump," International Journal of Heat and Fluid Flow, **29**, pp. 1527-1540.

[9] Furukawa, A., Takahara, H., et al, 2003, "Pressure fluctuation in a vaned diffuser downstream from a

centrifugal pump impeller," International Journal of Rotating Machinery, **9**, pp. 285-292.

[10] Arndt, N., Acosta, A. J., Brennen, C. E., Caughey T K, 1990, "Experimental investigation of rotor/stator interaction in a centrifugal pump with several vaned diffusers," ASME J. Turbomach., **111**, pp. 213-221.

[11] Eui, Y. K., Nam, H. C., 2001, "Experimental study on the mean flow characteristics of forward - curved centrifugal fans," KSME International Journal, **15**(12), pp. 1728-1738.

[12] Nakagawa, T., Furukawa, A., Takahara, H., 2001, "Flow behavior downstream of diffuser pump impeller," ASME J. Turbomach., **29**(2), pp. 110-118.

[13] Hong, S. S., Kang, S. H., 2004, "Flow at the centrifugal pump impeller exit with the circumferential distortion of the outlet static pressure," ASME J. Fluid Eng., **126**(1), pp. 81-86.

[14] Petit, O., Nilsson, H., 2013, "Numerical investigations of unsteady flow in a centrifugal pump with a vaned diffuser," International Journal of Rotating Machinery, **961580**.

[15] Wuibaut, G., Bois, G., et al, 2002, "PIV Measurements in the Impeller and the Vaneless Diffuser of a Radial Flow Pump in Design and Off-Design Operating Conditions," ASME J. Fluid Eng., **124**(3), pp. 791-797.

[16] Atif, A., Benmandsour, S., Bois, G., Dupont, P., 2011, "Numerical and experimental comparison of the vaned diffuser interaction inside the impeller velocity field of a centrifugal impeller," Science China, **1**(54), pp. 1-9.

[17] Dazin, A., Cavazzini, G., et al, 2011, "High-speed stereoscopic PIV study of rotating instabilities in a radial vaneless diffuser," Exp Fluids., **51**, pp. 83-93.

[18] Cavazzini, G., Pavesi, G., et al, 2009, "Analysis of the rotor-stator interaction in a radial flow pump," La Houille Blanche, **5**, pp. 141-151.

[19] Cavazzini G, Dupont P, et al, 2013, "Unsteady velocity PIV measurements and 3D numerical calculation comparisons inside the impeller of a radial pump model," *10th European Conference on Turbomachinery-Fluid Dynamics and Thermodynamics*, 15th -19th April, Lappenranta, Finland, pp. 1-9.

[20] Argüelles Díaz, K. M., Fernández Oro, J. M., et al, 2009, "Cylindrical three-hole pressure probe calibration for large angular range," Flow Measurement and Instrumentation, **20**, pp. 57-68.

[21] Barrand, J. P., Caignaert, G., Graesser, J. E., Rieutord, E., 1985, "Synthesis of the results of tests air and water aimed at critical re-circulating flow rates detections on the inlet and outlet of a centrifugal impeller," La Houille Blanche, **5**.

[22] Idel'Cik, I., 1960, *Mémento des pertes de charges singulières et de pertes de charges par frottements*, Eyrolles éditions.

[23] Bayeul-Lainé, A. C., Dupont, P., et al, 2013, "Fluid leakage effect on analysis of a vaned diffuser of SHF," *15th International Symposium on Transport Phenomena and Dynamics of Rotating Machinery*, February 24-28, 2014, Honolulu, HI, USA.

[24] Wuibaut, G., 2001, "Etude par vélocimétrie par images de particules des interactions roue-diffuseur dans une pompe centrifuge," Ph.D thesis, ENSAM, France.

[25] Simpson, R. L., 1996, "Aspects of turbulent boundary layer separation," Progess in Aerospace Sciences, **32**, pp. 457-52.
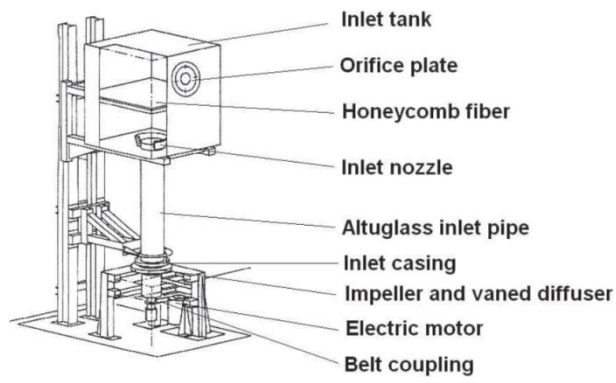
(a) Test loop of measurement system
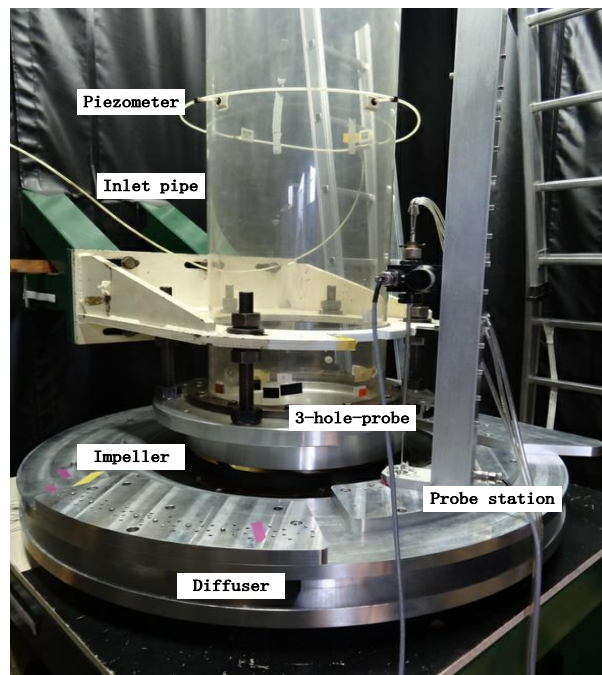
(b) Three-hole probe installation diagram
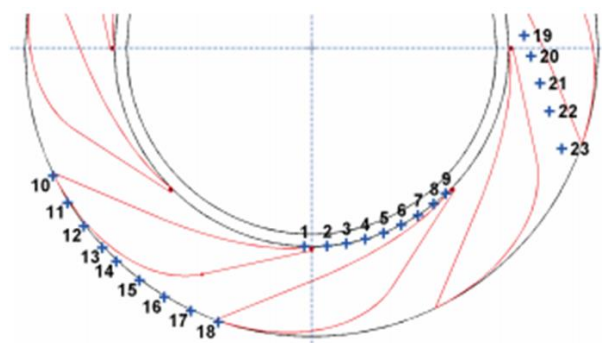
(c) Locations of probe traverses in the vane diffuser

Fig. 1 Test ring apparatus
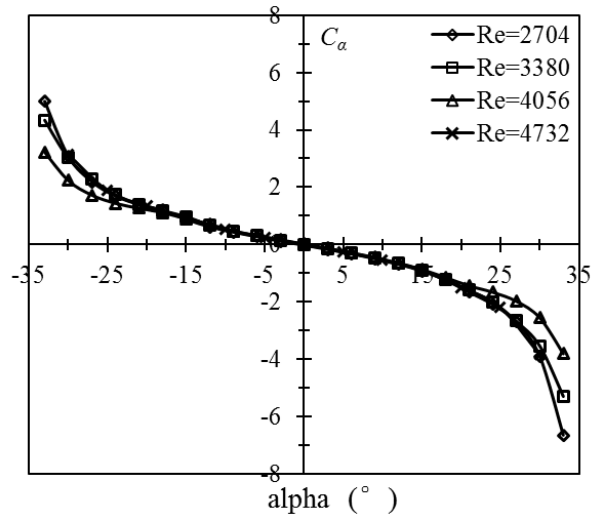
(a) Angle coefficient
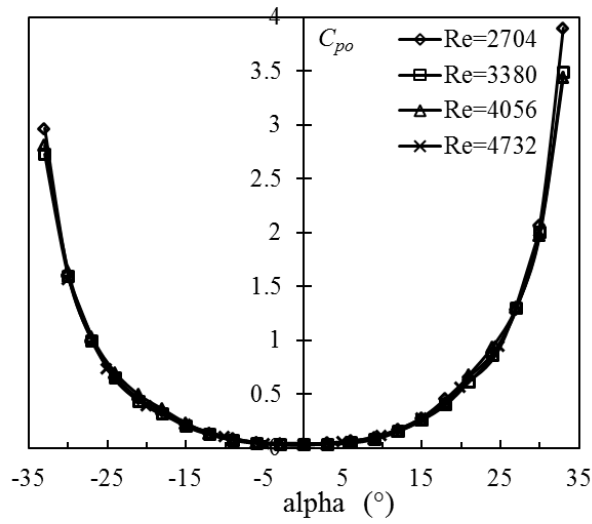
(b) Pressure coefficient
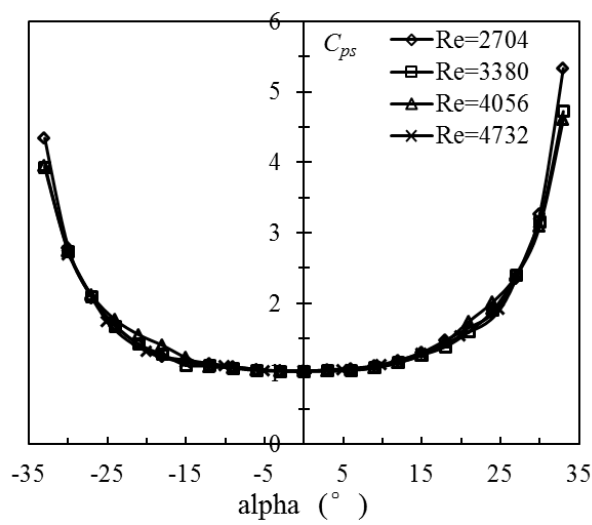
(c) Velocity coefficient

Fig. 2 Probe characteristics
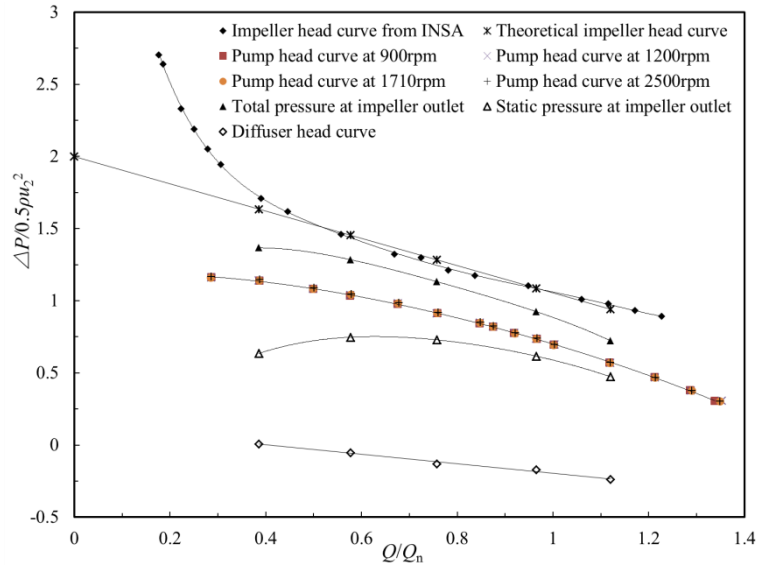
Fig. 3 Pump component head curves and respective flow rates
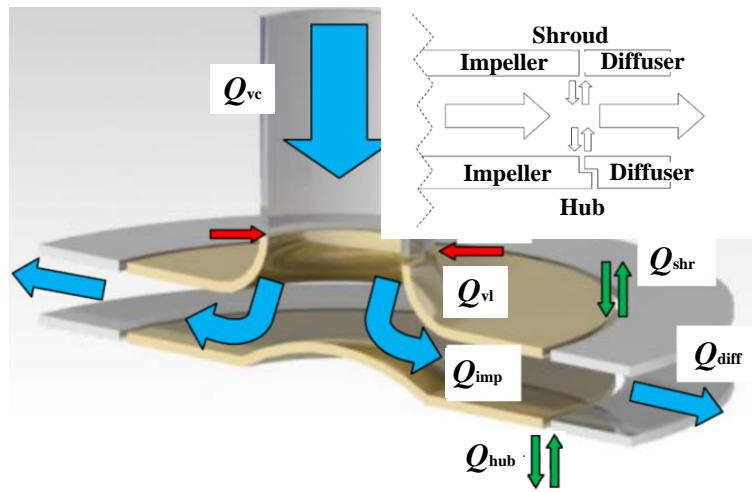
Fig. 4 Fluid leakage models
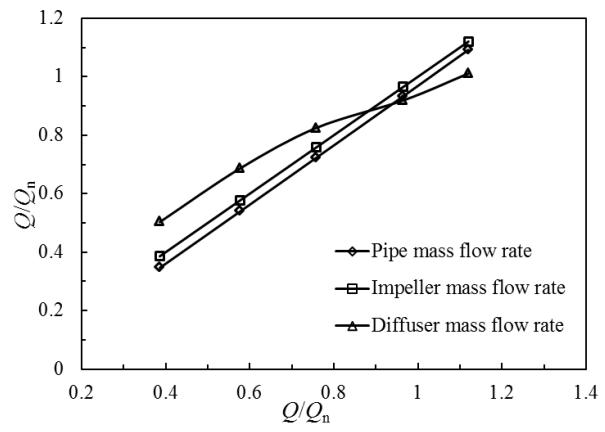
Fig. 5 Pump components flow rate
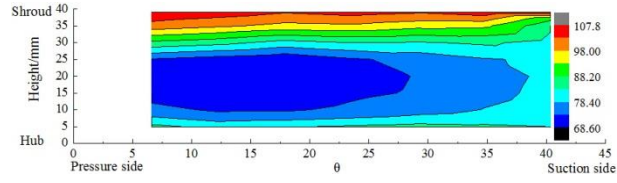
(a) $Q/Q_n = 0.386$
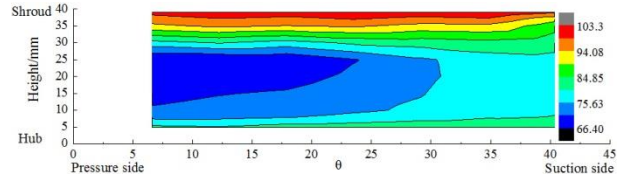
(b) $Q/Q_n = 0.581$
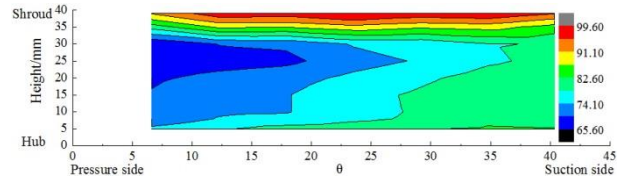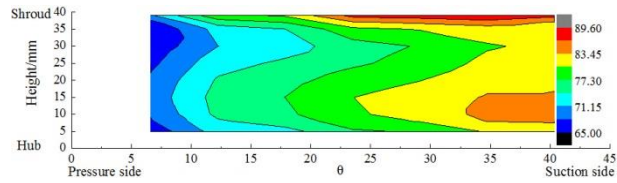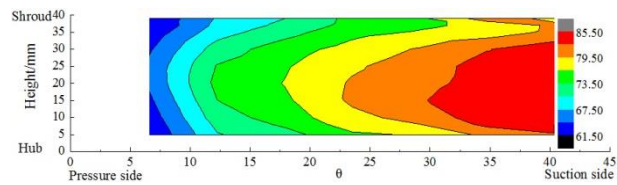
(c) $Q/Q_n = 0.762$

(d) $Q/Q_n = 0.968$

(e) $Q/Q_n = 1.12$

Fig. 6 Flow angle at R_3
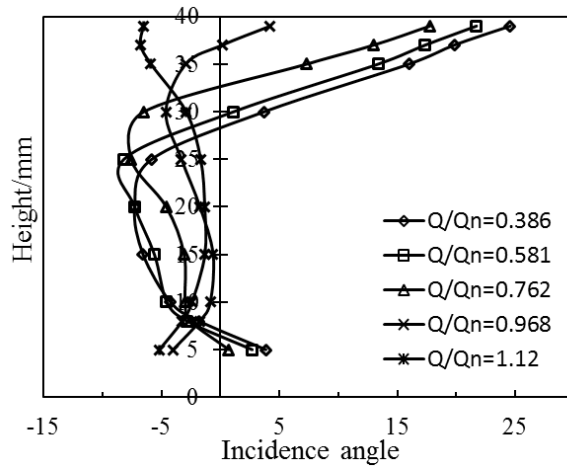
(a) Mean incidence flow angle
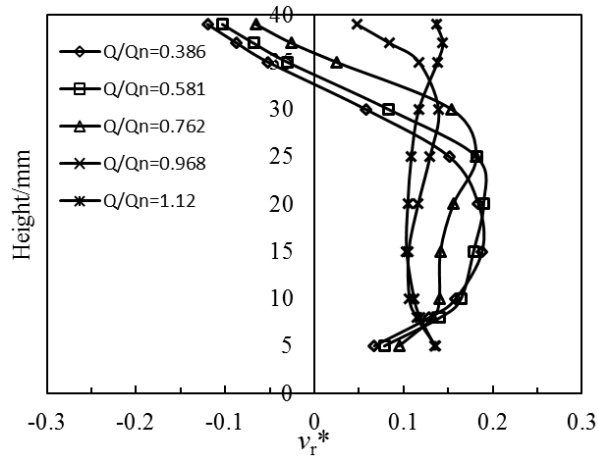
(b) Non-dimensional radial velocity

Fig. 7 Mean values at the inlet of the diffuser
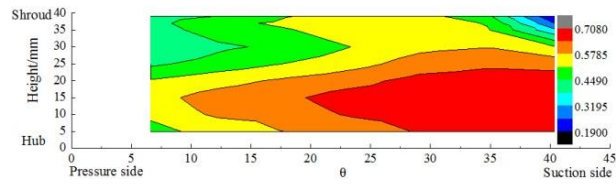
(a) $Q/Q_n = 0.386$
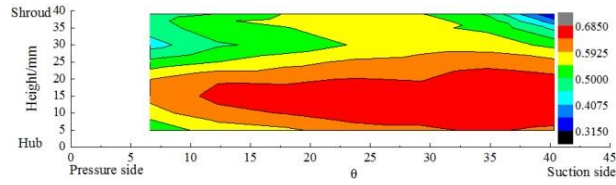
(b) $Q/Q_n = 0.581$
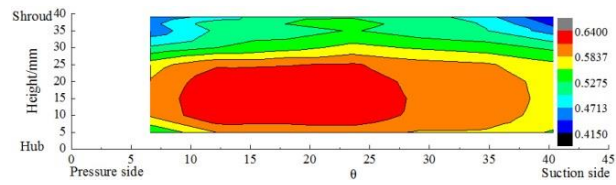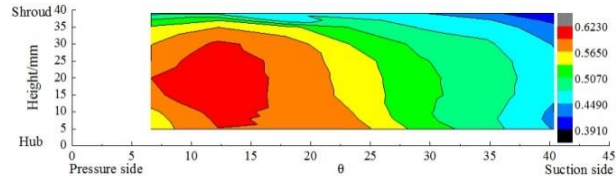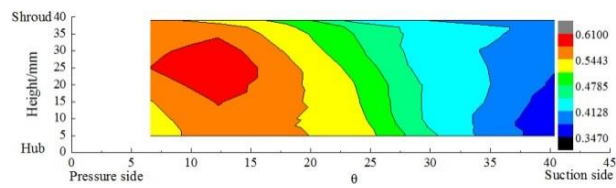
(c) $Q/Q_n = 0.762$

(d) $Q/Q_n = 0.968$

(e) $Q/Q_n = 1.12$

Fig. 8 Non-dimensional absolute velocities at R_3
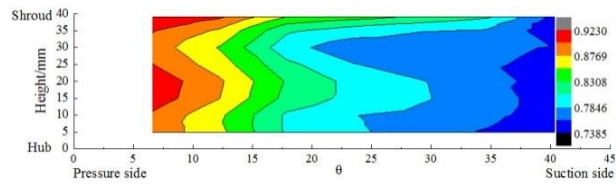
(a) $Q/Q_n = 0.386$
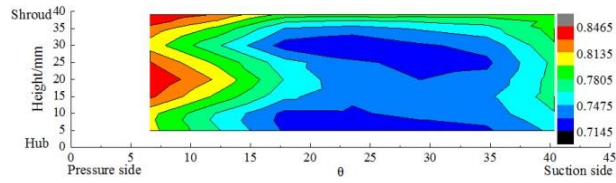
(b) $Q/Q_n = 0.581$
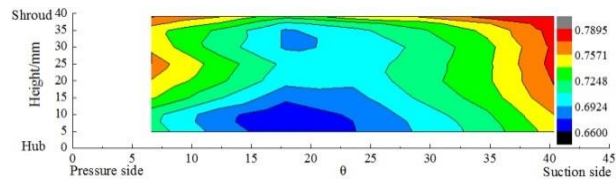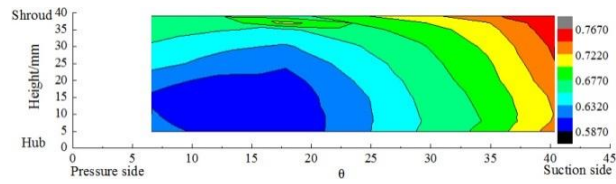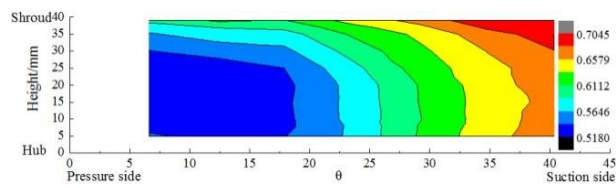
(c) $Q/Q_n = 0.762$

(d) $Q/Q_n = 0.968$

(e) $Q/Q_n = 0.1.12$

Fig. 9 Non-dimensional static pressure at R_3
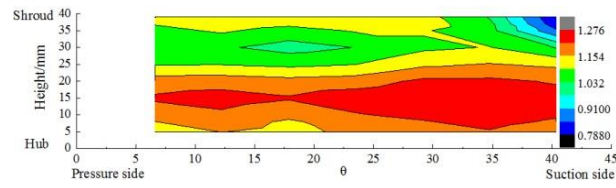
(a) $Q/Q_n = 0.386$
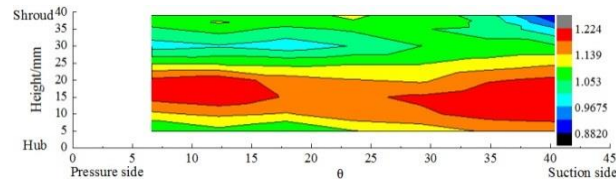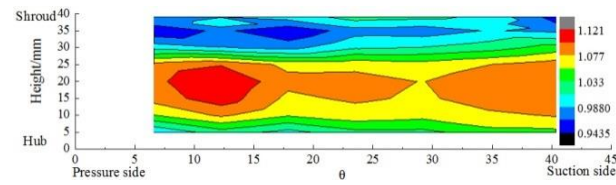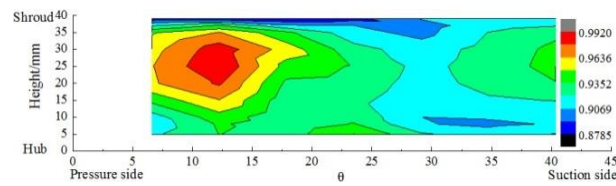
(b) $Q/Q_n = 0.581$
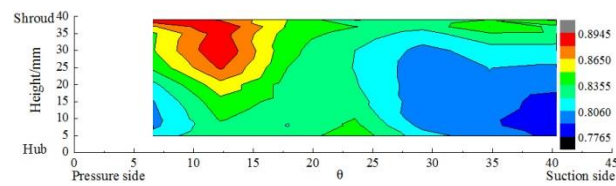
(c) $Q/Q_n = 0.762$

(d) $Q/Q_n = 0.968$

(e) $Q/Q_n = 1.12$

Fig. 10 Non-dimensional total pressure at R_3
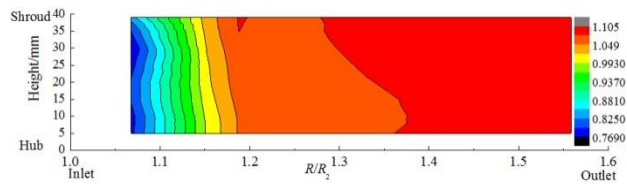
(a) $Q/Q_n = 0.386$
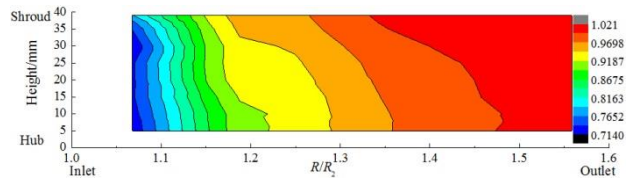
(b) $Q/Q_n = 0.581$
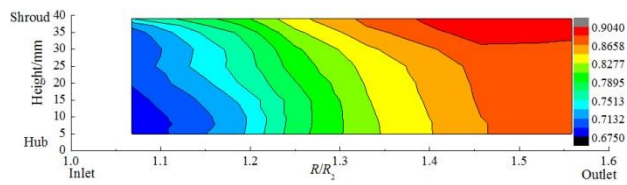
(c) $Q/Q_n = 0.762$
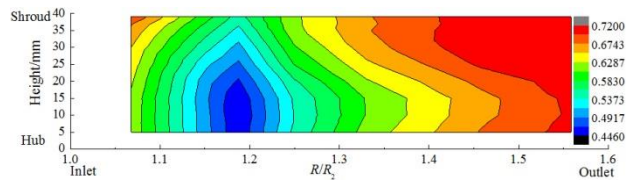
(d) $Q/Q_n = 0.968$
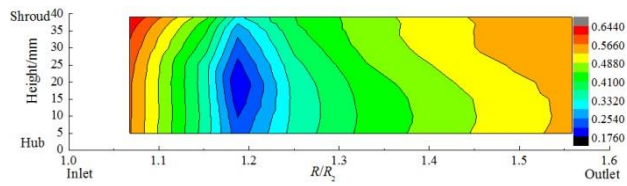
(e) $Q/Q_n = 0.1.12$

Fig. 11 Non-dimensional static pressure at the mean line
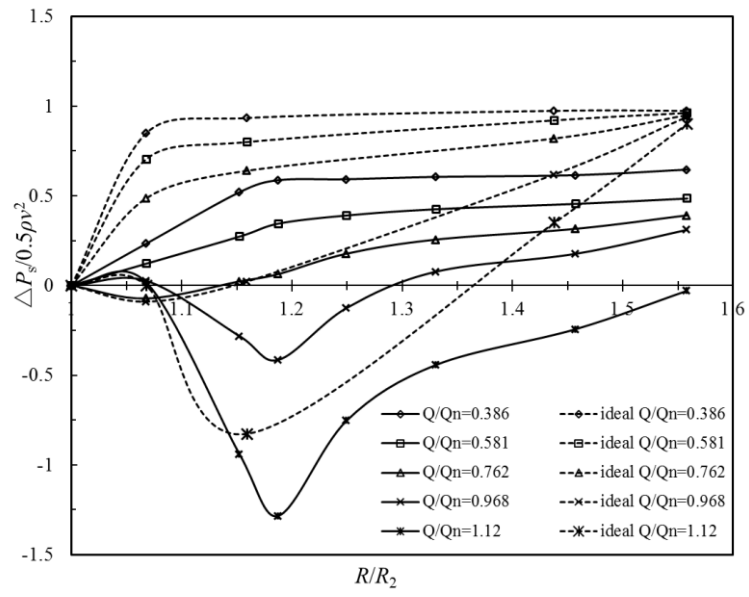
Fig. 12 Evolution of static pressure coefficient downstream of the impeller

$$(Y = [P_{sta}(R) - P_{sta}(R_2)]/(0.5 \times \rho v_2^2))$$
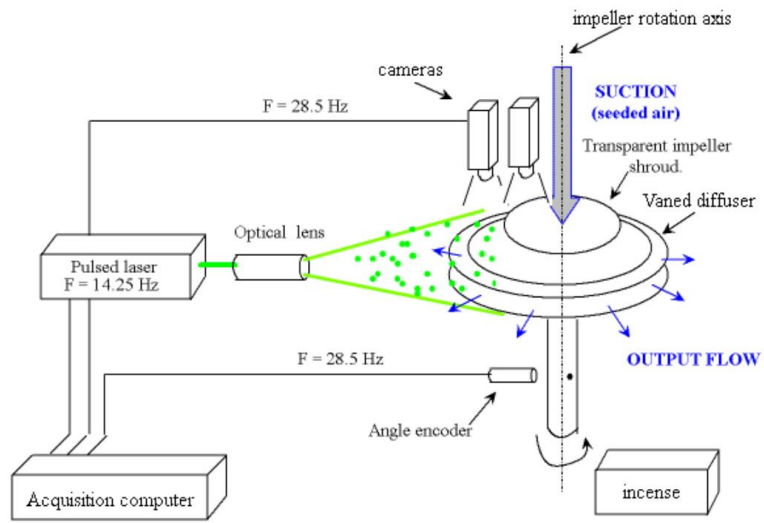
(a) PIV acquisition system
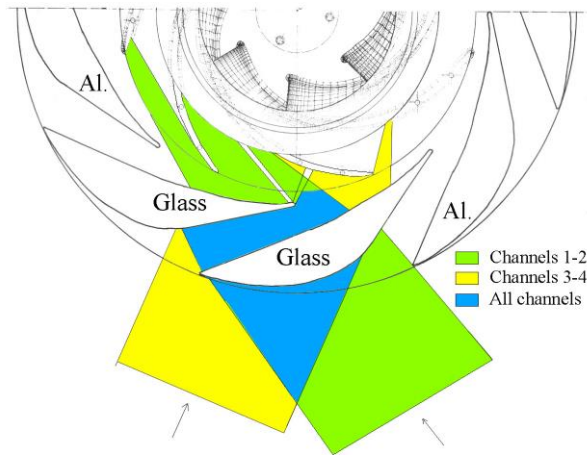
(b) Laser sheets
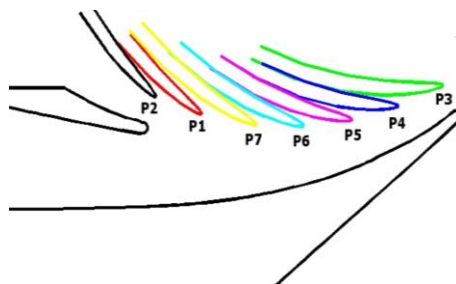
(c) Scheme of the impeller positions

Fig. 13 PIV acquisition system, measuring plans, and positions
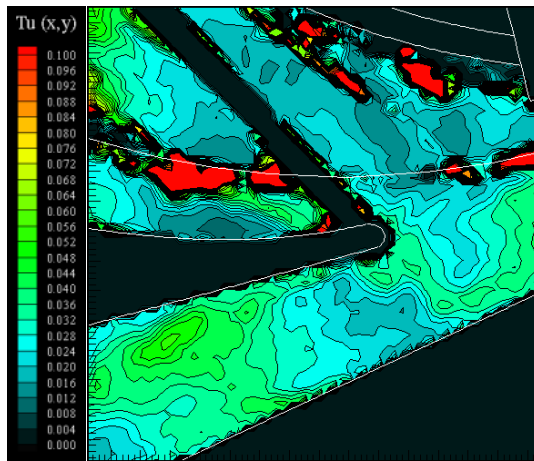
(a) $Q/Q_n = 0.581$
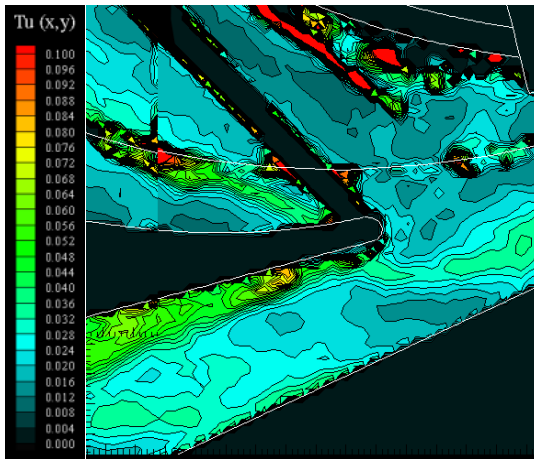
(b) $Q/Q_n = 0.762$
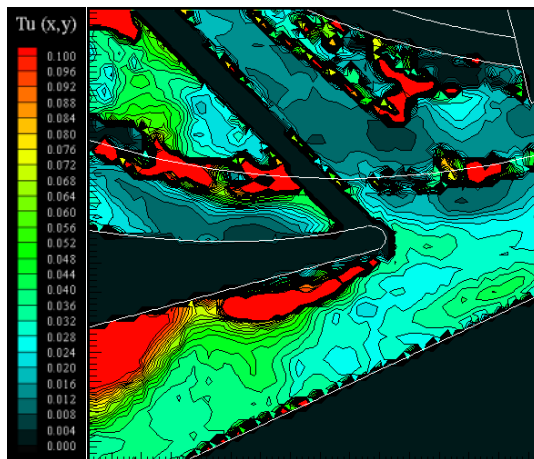
(c) $Q/Q_n = 1.12$

Fig. 14 Turbulence rate
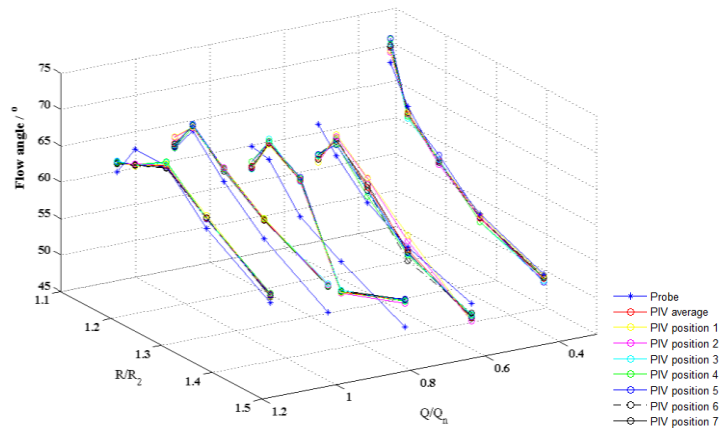
(a) Flow angle comparison
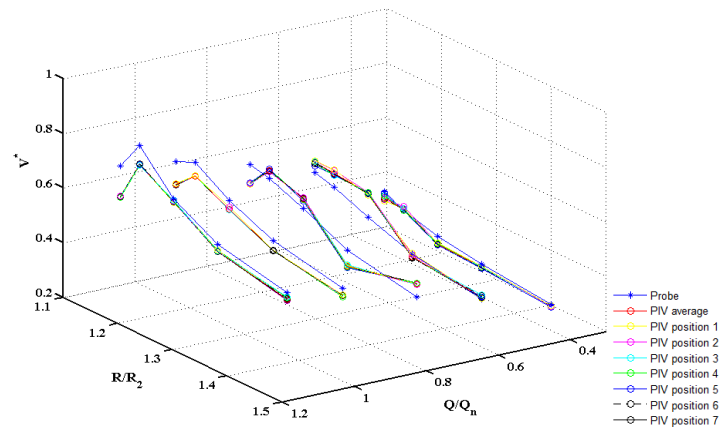
(b) Non-dimensional absolute velocity comparison

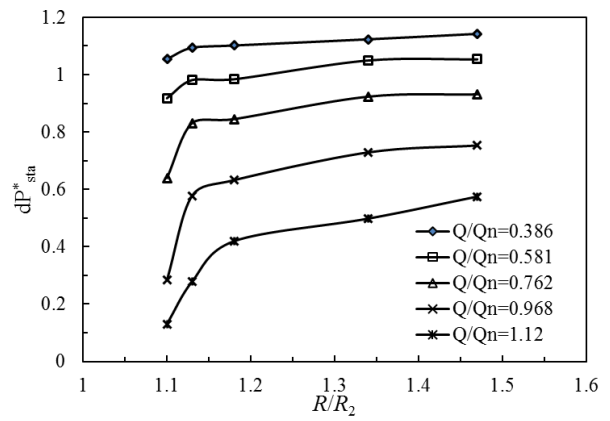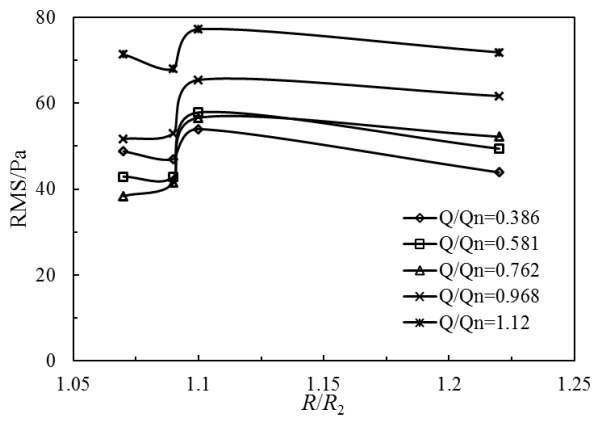Fig. 15 Comparison of the results between probe and PIV measurement at mid-span
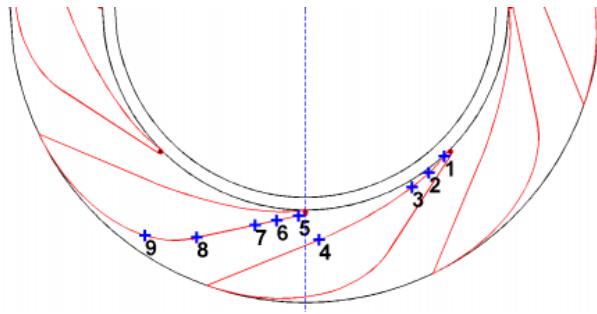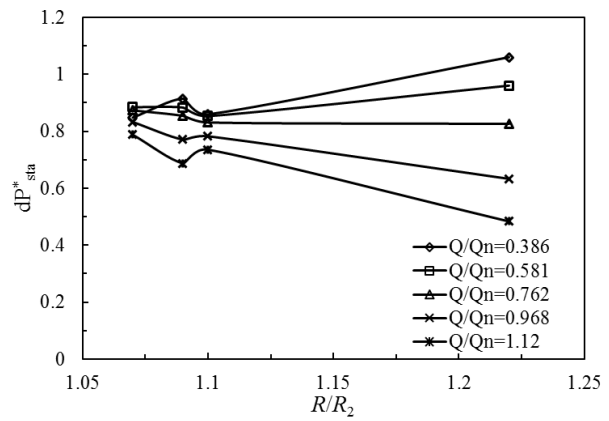
Fig. 16 Locations of pressure traverses in the vane diffuser
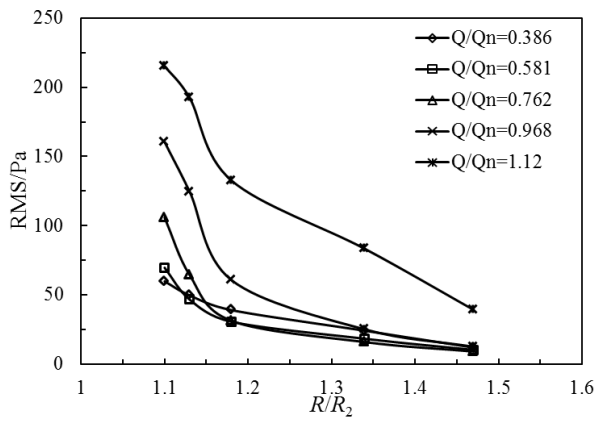
(a) RMS at the pressure side
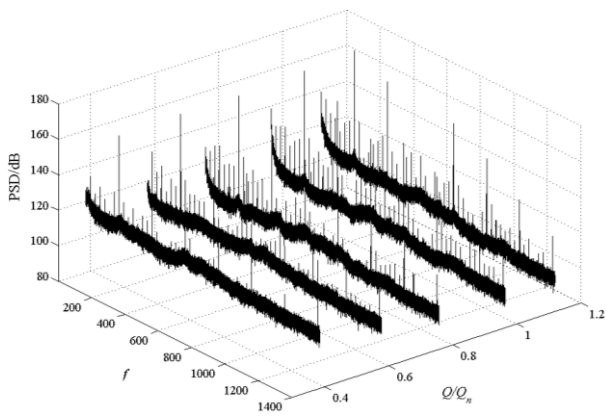
(b) Averaged $\mathrm{d}P^*_{sta}$ at the pressure side

(c) RMS at the suction side

(d) Averaged $\mathrm{d}P^*_{sta}$ at the suction side
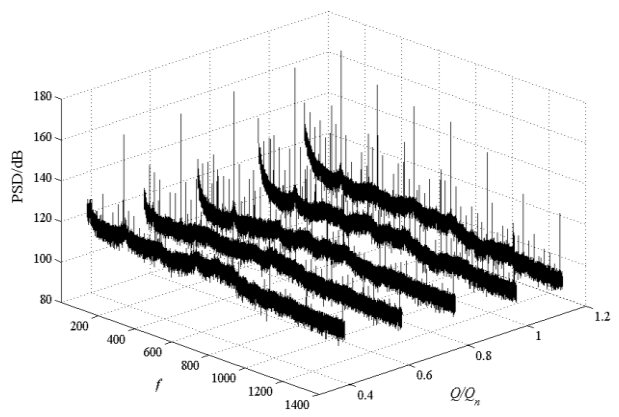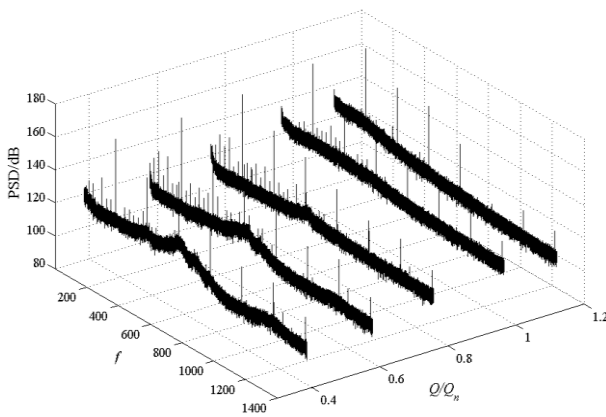
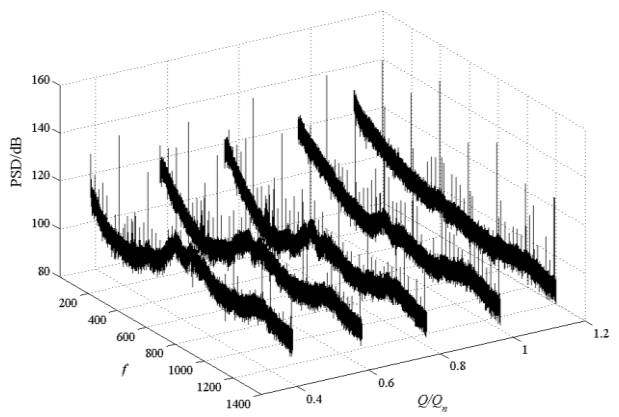Fig. 17 Statistical results of unsteady wall static pressure

(a) Point 2

(b) Point 4

(c) Point 6

(d) Point 9

Fig. 18 Auto PSD of the wall static pressure characteristic

Table 1 Parameters of the tested pump configurations

Impeller		
Inlet radius	R_1 (mm)	141.1
Outlet radius	R_2 (mm)	256.6
Outlet width	b_2 (mm)	38.5
Number of blades	Z_1	7
Outlet blade angle	β_{2a} (°)	22.30
Mean blade thickness	s (mm)	9
Speed	N (rpm)	1,710
Diffuser		
Inlet radius	R_3 (mm)	273.6
Outlet radius	R_4 (mm)	397.8
Constant width	B_4 (mm)	40
Number of blades	Z_2	8
Inlet blade angle	α_{31} (°)	10.21
Outlet blade angle	α_4 (°)	39.55
Relative radial gap	$(R_3 - R_2)/R_2$	6.65%

Table 2 Radial and tangential velocities distribution at $0.581Q_n$, mid-span

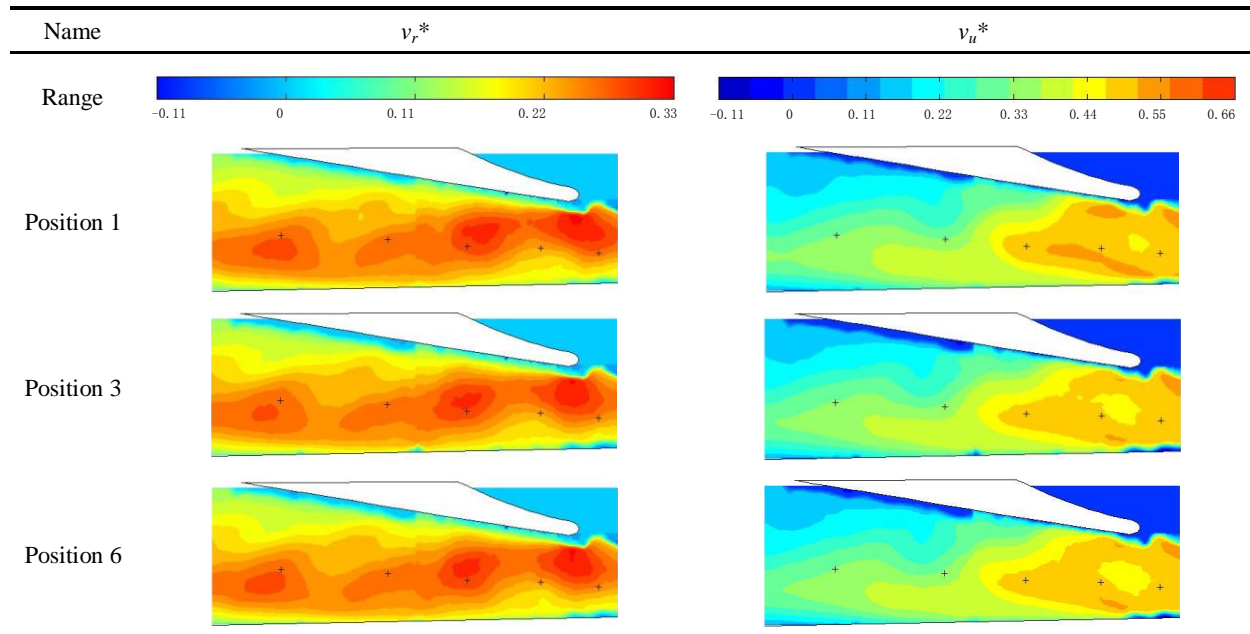| Name	v_r*	v_u*
Range		
Position 1		
Position 3		
Position 6		

Table 3 Contours of the mean velocity at several flow rates

Q/Q_n	v^*	v_r^*	v_u^*
0.386			
0.581			
0.762			
0.968			
1.12			